Acta Materialia 245 (2023) 118602

Contents lists available at ScienceDirect

Acta Materialia

journal homepage: www.elsevier.com/locate/actamat

Full length article

Strong and ductile refractory high-entropy alloys with super formability

Cheng Zhang [a], Haoren Wang [b], Xinyi Wang [c], Yuanbo T. Tang [d], Qin Yu [e,f], Chaoyi Zhu [f], Mingjie Xu [a], Shiteng Zhao [f], Rui Kou [g], Xin Wang [a], Benjamin E. MacDonald [a], Roger C. Reed [d], Kenneth S. Vecchio [b], Penghui Cao [c], Timothy J. Rupert [a], Enrique J. Lavernia [a,*]

[a] Department of Materials Science and Engineering, University of California Irvine, Irvine, CA 92697, USA
[b] Department of NanoEngineering, University of California San Diego, La Jolla, CA 92093, USA
[c] Department of Mechanical and Aerospace Engineering, University of California Irvine, Irvine, CA 92697, USA
[d] Department of Materials, University of Oxford, Parks Road, Oxford OX1 3PH, United Kingdom
[e] Materials Sciences Division, Lawrence Berkeley National Laboratory, Berkeley, CA 94720, USA
[f] Department of Materials Science and Engineering, University of California, Berkeley, CA 94720, USA
[g] Department of Structural Engineering, UC San Diego, La Jolla, CA 92093, USA

ARTICLE INFO

Keywords:
Refractory high-entropy alloys
Formability
Cryogenic-to-elevated temperatures
Strength-ductility synergy

ABSTRACT

Refractory high-entropy alloys (RHEAs) are considered promising candidate materials for high-temperature structural applications that currently use superalloys. However, for most of the reported RHEAs, their poor ductility and negligible cold-workability at room temperature have hindered their use. Here, we report a new class of non-equiatomic NbTaTi-based RHEAs that can be cold-rolled to a reduction of over 90% from the as-cast state without surface treatment and/or intermediate annealing. This excellent cold-workability is facilitated by activation of a high-density of dislocations and deformation twins as well as by high diffusivity paths, such that these RHEAs can be rendered homogeneous at lower annealing temperatures for much shorter time durations. In addition, we report that the RHEAs retain their high strength at elevated temperatures and exhibit considerable ductility at cryogenic conditions, evading the traditional strength–ductility trade-off. This class of super-formable RHEAs provides a novel design pathway to fabricate high-temperature structural materials via an energy- and time-saving method.

1. Introduction

As a new class of metallic materials, high-entropy alloys (HEAs) or complex concentrated alloys composed of four or more principal elements significantly expand the space of alloy design [1–3]. An increasing number of attractive properties have been discovered in HEAs over a wide temperature range, including excellent strength-ductility synergy at ambient temperature [4–6], exceptional mechanical properties at cryogenic temperatures [7], and ultrahigh strength at elevated temperatures [8]. Among various kinds of HEAs, refractory HEAs (RHEAs) stand out due to their unparalleled mechanical properties at high temperatures over 800 °C and even up to 1500 °C in some cases [9–11], which enables them to be promising candidates for high-temperature structural applications, outperforming conventional Ni-based superalloys. To date, a significant effort from the metallurgy community has focused on developing RHEAs with high processibility and outstanding strength-ductility synergy at ambient temperature. However, for most RHEAs, their ultra-high strength comes with very limited ductility [12,13]; as a result, tensile ductility is rarely reported for these alloys as it is commonly negligible. Furthermore, the poor cold-workability at room temperature makes the elimination of the as-cast microstructure difficult through conventional rolling and heat treatment processes, which greatly limits the application of RHEAs. For most of the reported RHEAs with reasonable ductility at room temperature, the mechanical properties were measured in their as-cast state [14–16], which is susceptible to stochastic premature failure due to casting defects including porosity, dendritic grain structure, and appreciable elemental segregation formed during the solidification process. For conventionally processed RHEAs, extended high-temperature homogenization (24–168 h at over $0.7T_m$, where T_m is the melting point) is needed for the as-cast samples to achieve a uniform microstructure due to extremely low diffusion rates for the alloy

* Corresponding author.
E-mail address: lavernia@uci.edu (E.J. Lavernia).

https://doi.org/10.1016/j.actamat.2022.118602
Received 20 July 2022; Received in revised form 8 November 2022; Accepted 7 December 2022
Available online 8 December 2022

constituents [8], a processing routine which is both time and energy intensive. Therefore, the design and fabrication of RHEAs with high processibility and good tensile strength-ductility synergy at room temperature remains a paramount challenge. Inspired by the HfNbTaTiZr (Senkov alloy) RHEA and some RHEAs derived from the original Senkov alloy, some criteria were put forward and subsequently revised to improve the ductility of RHEAs at room temperature [17–23]. The Senkov alloy processed through homogenization or surface treatment can indeed show good cold workability and tensile ductility at ambient temperature [24–33]. However, the surface treatment to remove casting defects, as reported in these studies, would result in a considerable material waste and cost increases [26,31,32].

In addition to designing new alloy compositions, the tailoring of internal microstructures provides an another effective approach to surmount the traditional strength-ductility tradeoff in metals and alloys, especially by the introduction of a heterogeneous microstructure [34,35]. For example, heterogeneous lamella (HL) structures [36], bimodal structures [37,38], and gradient structures [39,40] have been engineered with targeted microstructural heterogeneities to achieve high strength, while maintaining ductility in metallic materials. Engineering of microstructural heterogeneities can be implemented to promote delocalization of strain and enhancement of work hardening ability, which helps to prevent the early formation of necking during the plastic deformation [34]. Recently, HEAs with heterogenous microstructures have successfully achieved high strength-ductility synergy [41–43]. However, it is important to note that these studies only focus on face centered cubic (FCC) HEAs, which already generally have good processibility. The application of heterogeneous microstructures to body centered cubic (BCC) RHEAs has been rarely reported to date due to the significant difficulty in thermomechanical processing, which underscores the novelty of the present work.

2. Experimental procedures

2.1. Materials preparation

All Nb-25Ta-15Ti-based RHEA ingots were produced by arc-melting a mixture of high-purity raw materials (Nb, Ta, Ti, Hf, Zr, all over 99.9 wt.% purity) under an Ar atmosphere. In the arc-melter chamber, a high-purity Ti-getter was used to absorb residual oxygen before arc-melting raw materials. In order to promote homogeneity, each RHEA ingot was flipped and re-melted for 5–8 times. The weight of as-cast samples was between 30 and 70 g. Some as-cast samples were processed through conventional homogenization at 1250–1500 °C for 10–18 h for comparison with thermomechanical-processed samples. Some as-cast samples with thickness of 6–7 mm were processed through thermomechanical processing, including cold rolling with a reduction in thickness (RIT) up to 91%, annealing (900–1300 °C, 0.5–1 h) and water quenching.

2.2. Mechanical testing

Room-temperature tensile test samples with a gauge length of 18 mm and a cross-section of 3 × (0.5–0.7) (mm^2) were produced by electrical discharge machining (EDM). Before room-temperature tensile testing, samples were ground and polished to a mirror surface with SiC papers up to 4000 grit. "Loading-unloading-reloading" (LUR) cyclic tension tests were conducted to calculate the back-stress of samples with heterogeneous lamella (HL) structure. The strain rate in the current study is set to 1×10^{-3} s^{-1}. Microhardness of samples were measured by Vicker's hardness testing (Leica Hardness Testing Machine). Load and loading time for microhardness test were 500 gf and 15 s, respectively. At least 10 data points were used for each measurement of the reported values. Besides, the hardness of fine grain (FG) and ultrafine grain (UFG) regions were evaluated using KLA (formerly KEYSIGHT) G200 Nanoindenter. Load, loading time and holding time for the test were 50 mN, 5 s and 2 s, respectively. Four-point bending test was employed to measure the fracture toughness of cold-rolled $Hf_{15}Nb_{40}Ta_{25}Ti_{15}Zr_5$ and other ductile RHEAs. The stress-intensity factor K in the four-point bending test can be calculated by Eq. (1) [44,45]:

$$K = \frac{3PL}{BW^2}\sqrt{\pi a}\left[1.122 - \frac{1.121a}{W} + 3.740\left(\frac{a}{W}\right)^2 + 3.873\left(\frac{a}{W}\right)^3 - 19.05\left(\frac{a}{W}\right)^4 + 22.55\left(\frac{a}{W}\right)^5\right] \quad (1)$$

where P is the load, B is the thickness, W is the width, a is the crack size, $L = (S1–S2)/2$, with S1 and S2, the external (16 mm) and internal (10 mm) spans. The samples were pre-cracked to a crack length/width ratio, a/W~ 0.5, consistent with ASTM E399. Related dimensions of samples for the four-point bending test are shown in Table S1.

For $Hf_{15}Nb_{40}Ta_{25}Ti_{15}Zr_5$ RHEA samples, high temperature tensile tests were conducted using an Instron Eletro-Thermal Mechanical Testing (ETMT) system [46]. The samples were first machined by electric-discharge machining (EDM) into plate specimens with a cross-sectional area of 2 × (0.5–0.7) mm^2, which is followed by grinding with abrasive media up to 4000 grit to a mirror finish. A K-type thermocouple was spot-welded at the center of the specimen to monitor and control temperature during testing. Heating was achieved via the joule effect by direct current at 10 K/s. Water-cooled grips were placed 16 mm apart at both ends of the sample. A parabolic temperature distribution is established where the center is the hottest and both ends are at room temperature. A thermal equilibrium is obtained along the loading direction for approximately 3 mm at the center of the thermocouple. In this region deformation is localized and hence regarded as the gauge section. The strain measurement was employed by video extensometer based on digital image correlation method using an iMetrum Video Gauge software [46], where fine speckle patterns were generated by spaying high temperature paint on the specimen's surface prior each test. Deformation was made after one minute of isothermal holding at a strain rate approximately 10^{-3} s^{-1} and video data is stored at an acquisition frequency of 10 Hz and subsequently analyzed to trace speckle movement within the gauge. Since the testing was isothermal, the strain camera settings were adjusted to optimal imaging conditions prior each test to ensure speckle patterns are clearly visible even the material is glowing. The subsequent strain measurements were completed using the commercial software Video Gauge™, where a point-based approach was used to mimic traditional gauges. The above-mentioned experimental set-up was thoroughly documented in our previous work [46]. The current alloys were tested at 800, 900, 1000 and 1100 °C in air.

For cryogenic-temperature (−196 °C) tensile test in the liquid nitrogen, $Hf_{15}Nb_{40}Ta_{25}Ti_{15}Zr_5$ RHEA samples were cut by EDM to dimensions of 17 (length) × 1.5 (width) × (0.5–0.7) (thickness) (mm^3). During the test, samples were rinsed in the liquid nitrogen, and an extensometer was employed to measure the strain. The strain rate was 10^{-3} s^{-1}.

2.3. Materials characterization

The microstructure and grain orientation of the RHEA samples were characterized by a field-emission scanning electron microscopy (SEM, FEI Quanta3D) equipped with Oxford Instruments EDS and EBSD detectors. The Oxford Aztec (Tango) software was employed to measure the misorientation between deformation twins or microbands and the matrix. In addition, a Rigaku XRD (Cu K_α radiation, Smartlab) was used to detect phases. The microstructures were also characterized using a JEM-2100F transmission electron microscope (TEM) and a JEM-2800 TEM. Kernel average misorientation (KAM) maps for ultrafine grains and fine grains after tensile test at specific strains were achieved with the NanoMegas precession electron diffraction (PED) system that is installed

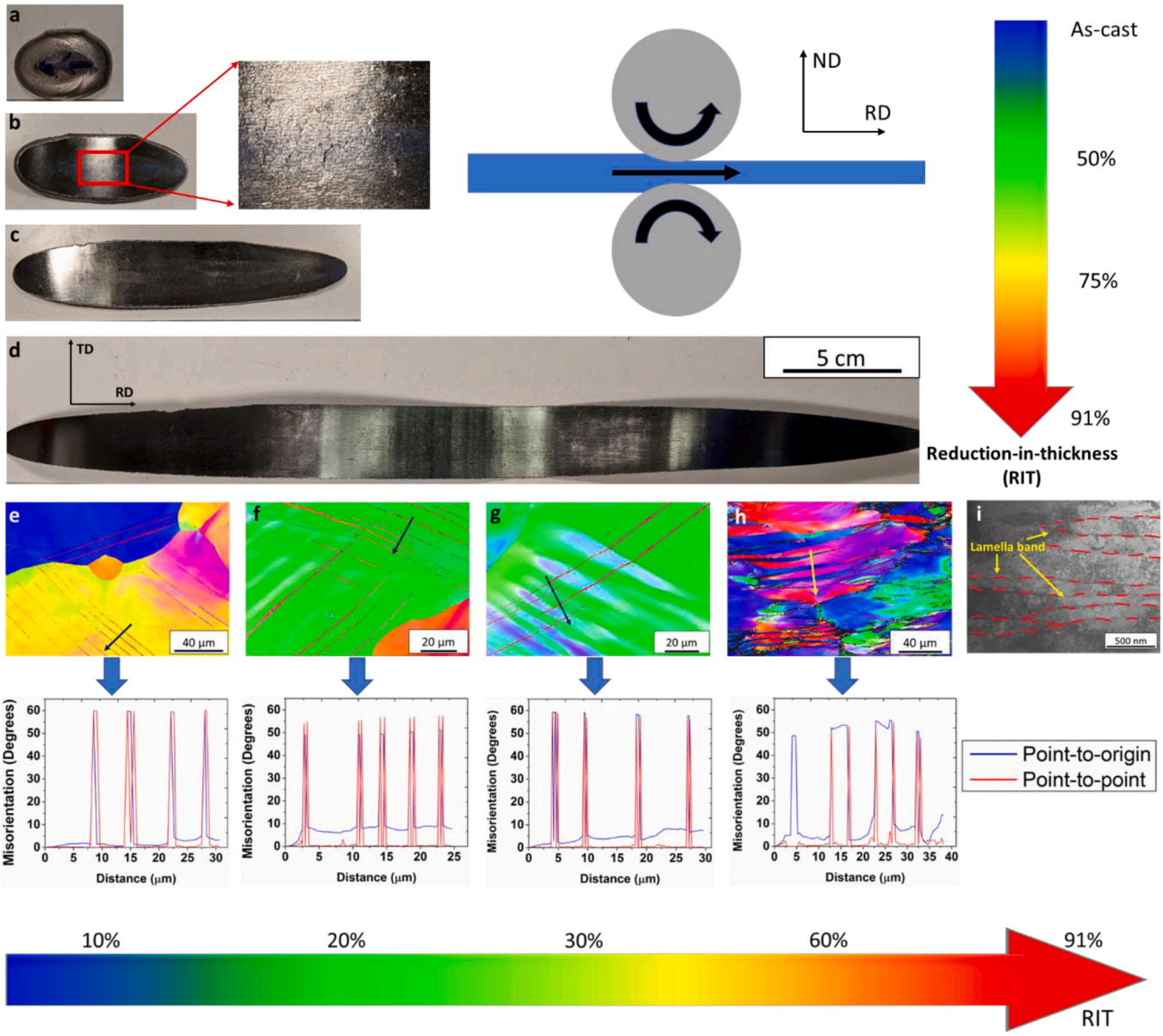

Fig. 1. Excellent cold-workability and the related deformed microstructure of $Hf_{15}Nb_{40}Ta_{25}Ti_{15}Zr_5$ RHEA at room temperature. Images of $Hf_{15}Nb_{40}Ta_{25}Ti_{15}Zr_5$ RHEA from (a) as-cast state to a reduction in thickness (RIT) of (b) 50% (some surface defects appear) (c) 75% and (d) 91%. Electron backscatter diffraction (EBSD) inverse pole figures (IPF) and related misorientation profiles of cold-rolled $Hf_{15}Nb_{40}Ta_{25}Ti_{15}Zr_5$ RHEA with RIT of (e) 10%, (f) 20%, (g) 30%, and (h) 60%. (i) Transmission electron microscopy (TEM) bright field (BF) micrograph of lamella bands with a high density of dislocations in NTTHZ RHEA with RIT of 91%. RD – rolling direction, ND- normal direction, TD – transverse direction.

in the JEM-2800 TEM. The TEM samples with a diameter of 3 mm were first mechanically ground to a thickness less than 50 μm. Then these discs were thinned through ion-milling to electron transparency using a Gatan PIPSII ion polishing system (Model 695).

2.4. Molecular dynamics (MD) simulation

A brick-shaped fragment of pure Nb is first created, with periodic boundary conditions along three orthogonal directions x = [100], y = [010], z = [001]. The initial aspect ratio of the brick-shaped configuration is 1:2:4, with dimensions ranging from $L_x \times L_y \times L_z$= 297A × 594A × 1188A (about 11 million atoms). To generate the alloying system, the Nb atoms are randomly selected and changed to Ta, Ti, which corresponds to an average composition $Nb_{60}Ta_{25}Ti_{15}$. 8 vacancy type prismatic loops (with burgers vectors of 1/2<111>) are inserted in to the Nb and $Nb_{60}Ta_{25}Ti_{15}$ system. We are using the embedded atom method (EAM) interatomic potentials developed by Zhou et al. [47] and Lin et al. [48] to model the interatomic interactions. The systems are compressed at a constant strain rate ($2e^9\ s^{-1}$) along the [001] axis, under constant temperature (300 K) using the isothermal, isobaric ensemble.

A second BCC simulation cell was created with three orthogonal axes along $x = [11\bar{2}]$, $y = [\bar{1}10]$, z= [111] with dimensions ranging from $L_x \times L_y \times L_z$ = 290A × 1160A × 580A. The procedures as aforementioned are applied. Crystals were compressed at a constant strain rate ($2e^9\ s^{-1}$) along with the $[\bar{1}10]$ axis. Dislocation extraction algorithm (DXA) and grain segmentation algorithm (GSA) in OVITO are used to reveal structural defects in simulated crystals [49].

The finite-element modeling for the evolution of surface defects in samples during the cold-rolling step was employed. Two-dimensional model is set up in COMSOL Multiphysics 5.3. A flat-end rigid plate is in contact with the top surface of $Hf_{15}Nb_{40}Ta_{25}Ti_{15}Zr_5$. The width W and the height H of the $Hf_{15}Nb_{40}Ta_{25}Ti_{15}Zr_5$ are set to be 40 mm and 7.2 mm,

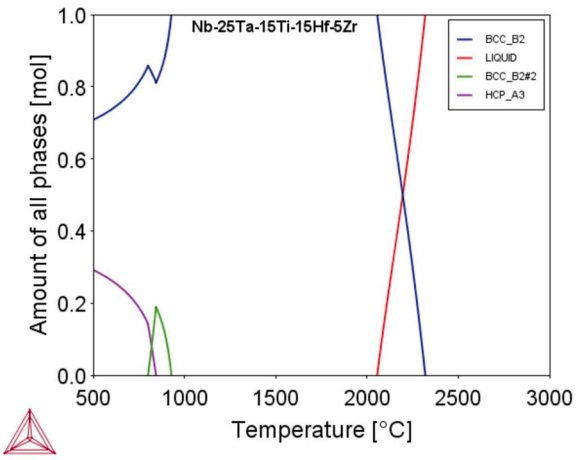

Fig. 2. CALPHAD result for $Hf_{15}Nb_{40}Ta_{25}Ti_{15}Zr_5$ RHEA, showing a high melting point around 2400 °C.

respectively. A triangular defect is located on the center top surface of the block. The bottom surface is fixed in the vertical direction; A downward vertical displacement is applied on the rigid plate. The contact between the indenter and $Hf_{15}Nb_{40}Ta_{25}Ti_{15}Zr_5$ is set to be frictionless. Before compression, the upper surface of the $Hf_{15}Nb_{40}Ta_{25}Ti_{15}Zr_5$ remains flat, and the rigid plate is contact with it with no applied force. Free Triangular mesh was employed. The material properties of $Hf_{15}Nb_{40}Ta_{25}Ti_{15}Zr_5$ are the same as the measurement data from tensile tests.

3. Results

3.1. Cold workability and related microstructure evolution

Our RHEA has a composition of $Hf_{15}Nb_{40}Ta_{25}Ti_{15}Zr_5$ (at %, termed as NTTHZ), is fabricated by arc-melting and can be cold-rolled directly from the as-cast state to a reduction in thickness (RIT) of over 90% without intermediate annealing, thus exhibiting excellent processability, as illustrated in Figs. 1(a–d) and S1. Such super formability is like that of the homogenized HfNbTaTiZr RHEA [24,25,29]. In addition, based on the CALPHAD results (see Fig. 2), the melting point of the NTTHZ RHEA is over 200°C higher than that of the Senkov alloy, indicating higher strength at elevated temperatures [11]. We first found that the matrix composition $Nb_{60}Ta_{25}Ti_{15}$ shows exceptional formability, while the addition of Hf up to 15 at % maintains cold-workability of the matrix ($Hf_{15}Nb_{45}Ta_{25}Ti_{15}$), while simultaneously strengthening the matrix (see Fig. S2). The addition of Hf can help to decrease valence electron concentration value of alloys, which may contribute to improve ductility in BCC RHEAs [19]. In previous work, as-cast equiatomic NbTaTi alloy exhibits good tensile properties [18,21], indicating similar cold workability to the current non-equiatomic $Nb_{60}Ta_{25}Ti_{15}$ matrix. During the cold-work process for NTTHZ RHEA, surface defects formed during the previous solidification step that can be eliminated by the subsequent cold rolling step (as shown in Figs. 1b and 3a), meaning that this material self-heals effectively during processing. Finite-element modeling is employed to understand this defect elimination, as shown in Fig. 3b, where compression processing is treated as the primary deformation mode during cold rolling. It is found that the stress concentration at the surface defects is always lower than the tensile ultimate stress of the sample, which prevents the growth of surface cracks. On the other hand, the tensile stress, caused by surface friction during the cold rolling step, helps to elongate samples mainly along the rolling direction, which makes surface cracks blunt progressively with increasing RIT. This behavior is unique, as other as-cast RHEAs with reasonable tensile ductility at ambient temperature [15] still fracture with RIT less than 40% (see Fig. S3), and also demonstrate lower fracture toughness than $Hf_{15}Nb_{40}Ta_{25}Ti_{15}Zr_5$ (see Fig. S4). In the cold rolling process for $Hf_{15}Nb_{40}Ta_{25}Ti_{15}Zr_5$, deformation-induced twins appear with RIT up to 60%, as shown in Fig. 1(e–h). Similar deformation-induced twinning was reported during compression deformation of HfNbTaTiZr RHEA in the temperature range from room temperature to 600 °C [50]. Some deformation-induced microbands or kink bands with misorientation less than 30° are also formed (see Figs. 1h and S5) with RIT of 30% and 60%. When the RIT reaches 80%, some shear bands appear (see Fig. S6). Eventually, with a larger RIT of 91%, the surface defects completely disappear. The formation of deformation twins and deformation-induced microbands contribute to the suppression of surface crack propagation, which is similar to the effect of nano-twins on improving fracture resistance in the Cantor alloy at cryogenic temperatures [7].

With a RIT over 90%, some nano-scale bands with a high-density of dislocations appear (Fig. 1i), which are similar to lamella bands formed in severely cold-rolled FCC metals or alloys with high/medium stacking

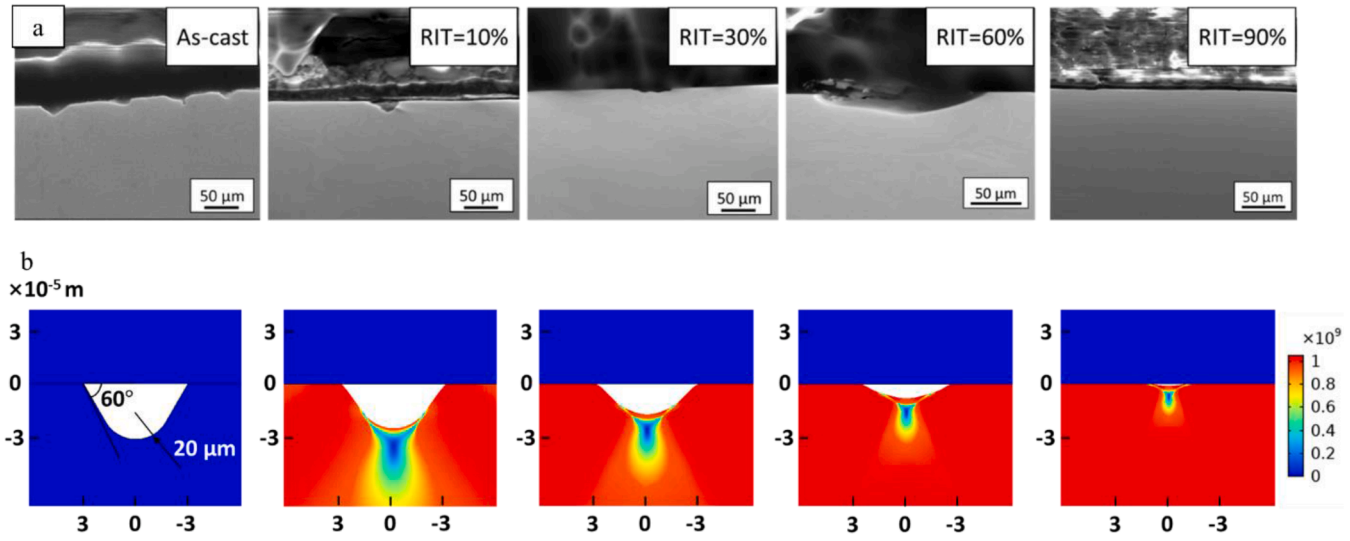

Fig. 3. Surface development of cold-rolled $Hf_{15}Nb_{40}Ta_{25}Ti_{15}Zr_5$ and related finite-element (FE) modeling, showing a unique process-healing phenomenon. (a) Evolution of surface defects in cold-rolled $Hf_{15}Nb_{40}Ta_{25}Ti_{15}Zr_5$ RHEA from the as-cast state to a RIT of 90%. (b) FE modeling for stress applied in the tip area of defects, unit: Pa.

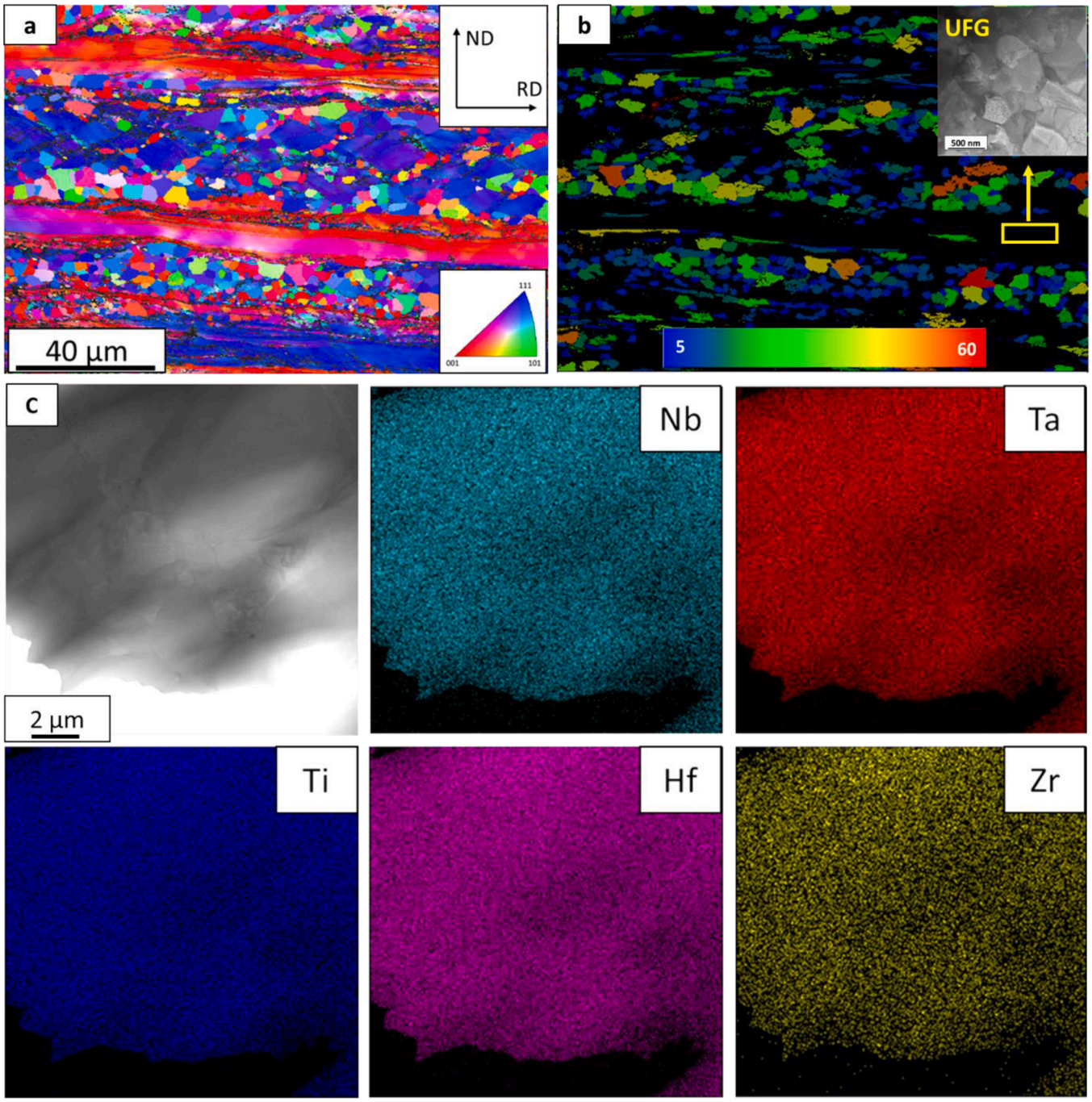

Fig. 4. Microstructure and related element distribution in $Hf_{15}Nb_{40}Ta_{25}Ti_{15}Zr_5$ RHEA with heterogeneous lamella (HL) structure. (a) EBSD inverse pole figure of $Hf_{15}Nb_{40}Ta_{25}Ti_{15}Zr_5$ RHEA after cold rolling with RIT of 90% and annealing at 900 °C for 1 h. (b) Corresponding grain area map of fully-recrystallized fine grains with grain area larger than 5 μm^2. Ultrafine grains (UFGs) in the recovery state are distributed in the black areas. (c) Scanning TEM micrograph and related EDS mapping of ultrafine and fine grains in the rolled and annealed $Hf_{15}Nb_{40}Ta_{25}Ti_{15}Zr_5$, showing no element segregation. RD – rolling direction, ND – normal direction.

fault energies [51,52]. It is also interesting to note that the hardness of the sample maintains at a high value (~350 Vickers hardness) during the cold-rolling process when RIT is over 30% (see Fig. S7a), while the microhardness usually increases with RIT more rapidly for FCC HEAs with large RIT above this value. In addition, the microhardness of cold-rolled samples even slightly decreases when RIT increases from 30% to 60%, providing evidence of a softening phenomenon. Based on the misorientation profiles in Fig. 1(e–h), the deformation-induced twins with 60^o misorientation are from the {112}<111> twin system, while those with approximately 50^o misorientation are associated with the {332}<113> twin system. With RIT increasing from 30% to 60%, more and more deformation-induced kink bands are formed, while fewer twins are observed. These kink bands contribute to softening and formability of specimens via stress relaxation and crystal reorientation, which is also observed in β-Ti alloys, pure Ti, and the Senkov alloy [53–55,29].The phases present in the cold-rolled $Hf_{15}Nb_{40}Ta_{25}Ti_{15}Zr_5$ RHEA were also checked after rolling, and it was confirmed that this alloy remained a single BCC structure (Fig. S7b). The microhardness development of the cold-rolled $Hf_{15}Nb_{40}Ta_{25}Ti_{15}Zr_5$ RHEA is like that of the Senkov alloy in the severe cold-rolled state, where further cold rolling (from RIT of 65% to RIT of 86%) did not result in significant additional changes in the Senkov alloy [24].

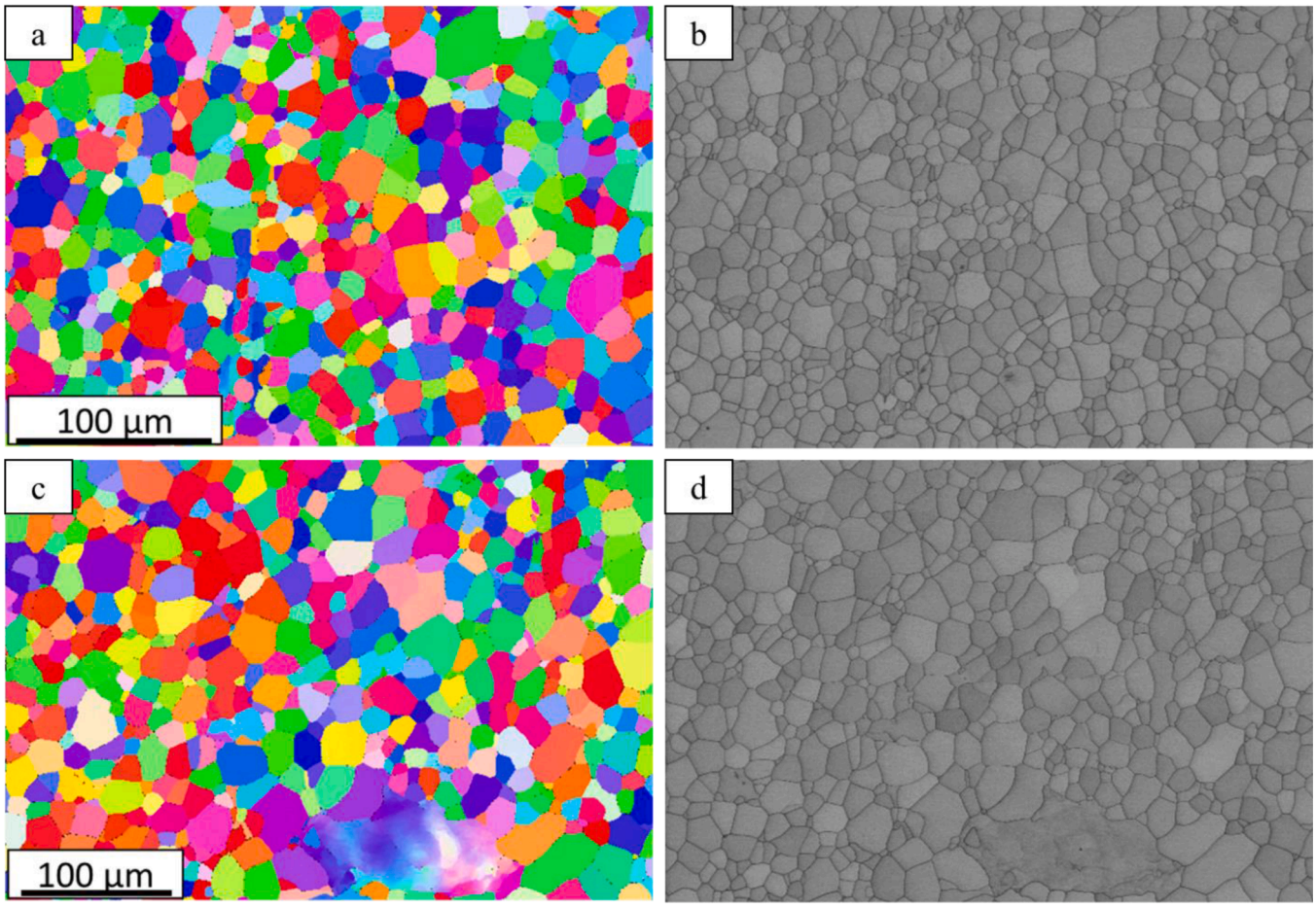

Fig. 5. EBSD inverse pole figures and related band contrast images for cold-rolled $Hf_{15}Nb_{40}Ta_{25}Ti_{15}Zr_5$ RHEA with different microstructures after annealing at different conditions. (a) EBSD IPF for CR90 $Hf_{15}Nb_{40}Ta_{25}Ti_{15}Zr_5$ RHEA after annealing at 1150 °C for 1 h. (b) Related EBSD BC image for (a), showing a fine-grained microstructure. (c) EBSD IPF for CR90 $Hf_{15}Nb_{40}Ta_{25}Ti_{15}Zr_5$ RHEA after annealing at 1300 °C for 0.5 h. (d) Related EBSD BC image for (c), showing a coarse-grained microstructure.

3.2. Tunable microstructure

Furthermore, the microstructure of the cold-rolled $Hf_{15}Nb_{40}Ta_{25}Ti_{15}Zr_5$ RHEA can be tailored by controlling the annealing conditions. After annealing at different temperatures for short times from 0.5 to 1 h, an HL structure (shown in Fig. 4a,b), fine grains (Fig. 5a,b) (FG, grain size~ 9.9 μm), and coarse grains (Fig. 5c,d) (CG, grain size~ 22.8 μm) can be formed inside $Hf_{15}Nb_{40}Ta_{25}Ti_{15}Zr_5$. The HL structure is composed of ultrafine-grained (UFG, grain size~ 0.7 μm) region and fine-grained (grain size~ 4.4 μm) region, where microhardness in the UFG area is much higher than that in FG area, as shown in Fig. S8. Due to the high-density of dislocations formed during severe cold rolling (Fig. 1i), atoms can diffuse along dislocations during annealing with a much higher diffusion rate (i.e., dislocation pipe diffusion rather than conventional lattice diffusion through a random walk mechanism [56, 57]. Therefore, cold-rolled $Hf_{15}Nb_{40}Ta_{25}Ti_{15}Zr_5$ RHEA samples can be made homogeneous at a much lower annealing temperature (900 or 1150 °C) and with shorter annealing times (1 h) (Figs. 4c and S9) when compared with conventional homogenization steps for RHEAs with the same matrix (Nb-25Ta-15Ti-based) (1500 °C, over 12 h) (Fig. S10) or other similar RHEAs (HfNbTiTaZr, hot isostatically pressed for 2 h at 1200 °C and then annealed at 1200 °C for 24 h or annealed at 1800 °C for 6–192 h) [25,58,29] in the as-cast state. This unique feature of the NTTHZ RHEA reported herein, saves both time and thermal energy during processing, greatly reduces the barrier for utilization of this alloy and consequently increases the potential for widespread industrial use.

3.3. Tensile properties in a broad temperature range

The $Hf_{15}Nb_{40}Ta_{25}Ti_{15}Zr_5$ RHEA alloys not only have excellent cold-workability in the as-cast state, but also good tensile strength-ductility synergy in the annealed state when tested at ambient-to-elevated temperatures. In the true stress-strain curves shown in Fig. 6a, the $Hf_{15}Nb_{40}Ta_{25}Ti_{15}Zr_5$ RHEA with an HL structure can achieve a yield strength over 920 MPa and a failure elongation over 0.15 at room temperature, which is much stronger than the FG sample and at the same time remain as ductile as the CG sample. The mechanical properties of the FG and CG samples are similar to that of the as-cast NbHfTiZr RHEA [59]. The fracture surfaces of HL- NTTHZ RHEA samples are presented in Fig. 6b,c, which clearly show transgranular ductile fracture. Fig. 7 shows the strain hardening rate curves for $Hf_{15}Nb_{40}Ta_{25}Ti_{15}Zr_5$ RHEA samples with different microstructures. Even with a finer heterogeneous structure and higher strength, the HL-NTTHZ specimens can maintain a high strain hardening rate that is similar to the CG specimens until fracture takes place.

4. Discussion

4.1. Deformation mechanism during cold rolling

Atomistic simulations of uniaxial compression along two different orientations, [$\bar{1}$10] and [001] are performed to elucidate the deformation mechanisms in Nb-$Ta_{25}Ti_{15}$ alloy and pure Nb and understand the role of high concertation Ta and Ti solute atoms. When compressing

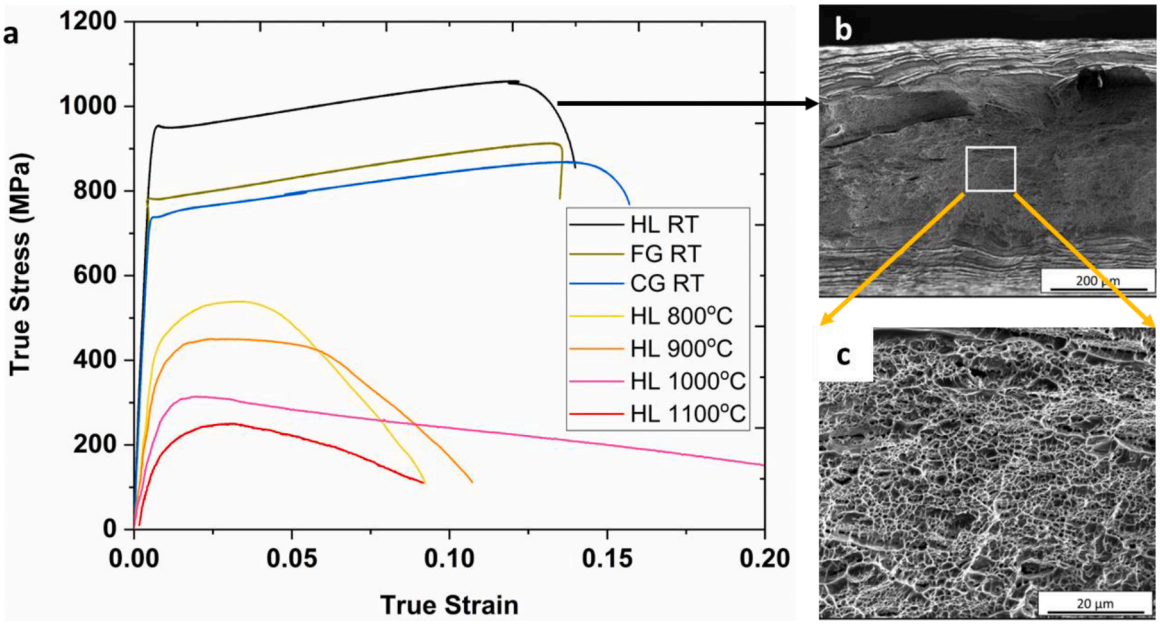

Fig. 6. High tensile strength-ductility synergy achieved in $Hf_{15}Nb_{40}Ta_{25}Ti_{15}Zr_5$ RHEA with HL structure at ambient-to-elevated temperatures. (a) True stress-strain (SS) curves of $Hf_{15}Nb_{40}Ta_{25}Ti_{15}Zr_5$ RHEA with HL structure at ambient temperature and elevated temperatures (800, 900, 1000 and 1100 °C). Related SS curves of specimens with fine grains (FG) and coarse grains (CG) tested at room temperature are also shown. SEM micrographs for the fracture surfaces of HL- NTTHZ RHEA after tensile test at room temperature, showing a high density of dimples and ductile fracture type in (b) and (c).

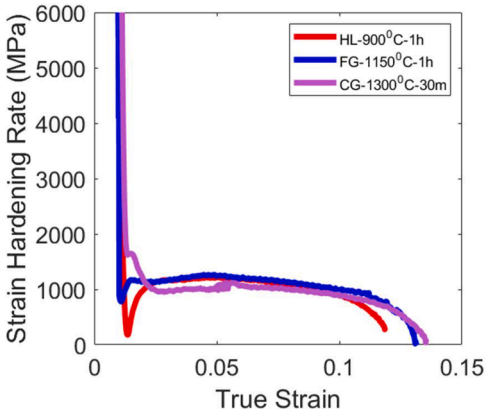

Fig. 7. Strain hardening rate curves of $Hf_{15}Nb_{40}Ta_{25}Ti_{15}Zr_5$ RHEA with different microstructures tested at room temperature.

along the [$\bar{1}$10] direction, $Nb_{60}Ta_{25}Ti_{15}$ yields by deformation twinning, involving a reorientation of the crystal lattice within twinned volumes of the materials (Fig. 8a). Twin embryos nucleate right after yielding and grow rapidly with increasing the applied strain, which fills large fractions of material volume. For [001] orientation, deformation-twins also nucleate in $Nb_{60}Ta_{25}Ti_{15}$ but only grow to a certain size, as shown in Fig. 8b. They are constrained from further growth by the surrounding dense dislocation networks, in which the predominant deformation mechanism in the system is dislocation slip. The orientation-dependent twinning can be interpreted by the twinning mechanism that occurs due to shear in <111> directions on {112} planes, and the twinning stress resolved from the compressive loading is dependent on loading orientations. It is interesting to note that, when comparing with $Nb_{60}Ta_{25}Ti_{15}$, twinning deformation and twin growth in pure Nb are drastically reduced, especially for [001] orientation compression, where stable twins do not occur (Fig. 8c). Compared with pure Nb, the abundant twins in Nb-$Ta_{25}Ti_{15}$ alloy signify the role of solutes in promoting twinning. This may originate from the atomic misfit strain and solid solution strengthening, giving rise to plastic flow stress above the critical value for activating twinning deformation. It is noted that $Nb_{60}Ta_{25}Ti_{15}$ is our base alloy composition that shows exceptional formability. The aim of the atomistic simulation is to reveal the role of concentrated solid solutions (mixing of Nb, Ta, and Ti, the three base elements in our alloys) on deformation mechanisms by comparing them to pure Nb. As illustrated in Fig. 8, the addition of Ta and Ti (i.e., $Nb_{60}Ta_{25}Ti_{15}$) promotes twinning deformation. It is reasonable to speculate that further addition of Hf and Zr would influence twinning as its effect on stacking faulty energy modulation. The relationship between composition, stacking faculty energy, and twinning propensity deserve further and careful study.

4.2. Comparison of mechanical property at elevated temperatures

In addition to room temperature performance, it is helpful to remember why RHEAs are intriguing in the first place: *the promise of great strength at high temperature*. Therefore, we compare the tensile strength of the $Hf_{15}Nb_{40}Ta_{25}Ti_{15}Zr_5$ RHEAs with Ni-based superalloys [60–65], refractory metals [61], and Nb-based and Ta-based refractory alloys [61,66] at elevated temperatures in Fig. 9, which further demonstrates the potential of our $Hf_{15}Nb_{40}Ta_{25}Ti_{15}Zr_5$ RHEA for high-temperature applications. When comparing with some most widely used Ni-based superalloys like Inconel 625 and Inconel 718 for disk use, the tensile strength of the $Hf_{15}Nb_{40}Ta_{25}Ti_{15}Zr_5$ RHEA is almost twice and three times higher at 900 °C and 1000 °C, respectively. In addition, although some Ni-based superalloys like Mar-247, CMSX-2, CMSX-4 and CMSX-10 which were designed for blade applications show exceptional strength below 1000 °C, their strength drastically decreases once the temperatures are over 1000 °C, which is shown as the blue oval in Fig. 9. The current NTTHZ RHEA shows comparable strength to those of CMSX-4 and CMSX-10 when the temperature reaches 1100 °C. In the case of CMSX-4 and CMSX-10, a high content of Ta is added to strengthen the matrix and increase the volume fraction of γ' with $L1_2$ structure. W element is added to improve the thermal stability of the alloy and strengthen the matrix. Moreover, a considerable amount of expensive Re (3–7 wt.%) is added to ensure good mechanical properties at elevated temperatures. However, their melting points (~1300 °C)

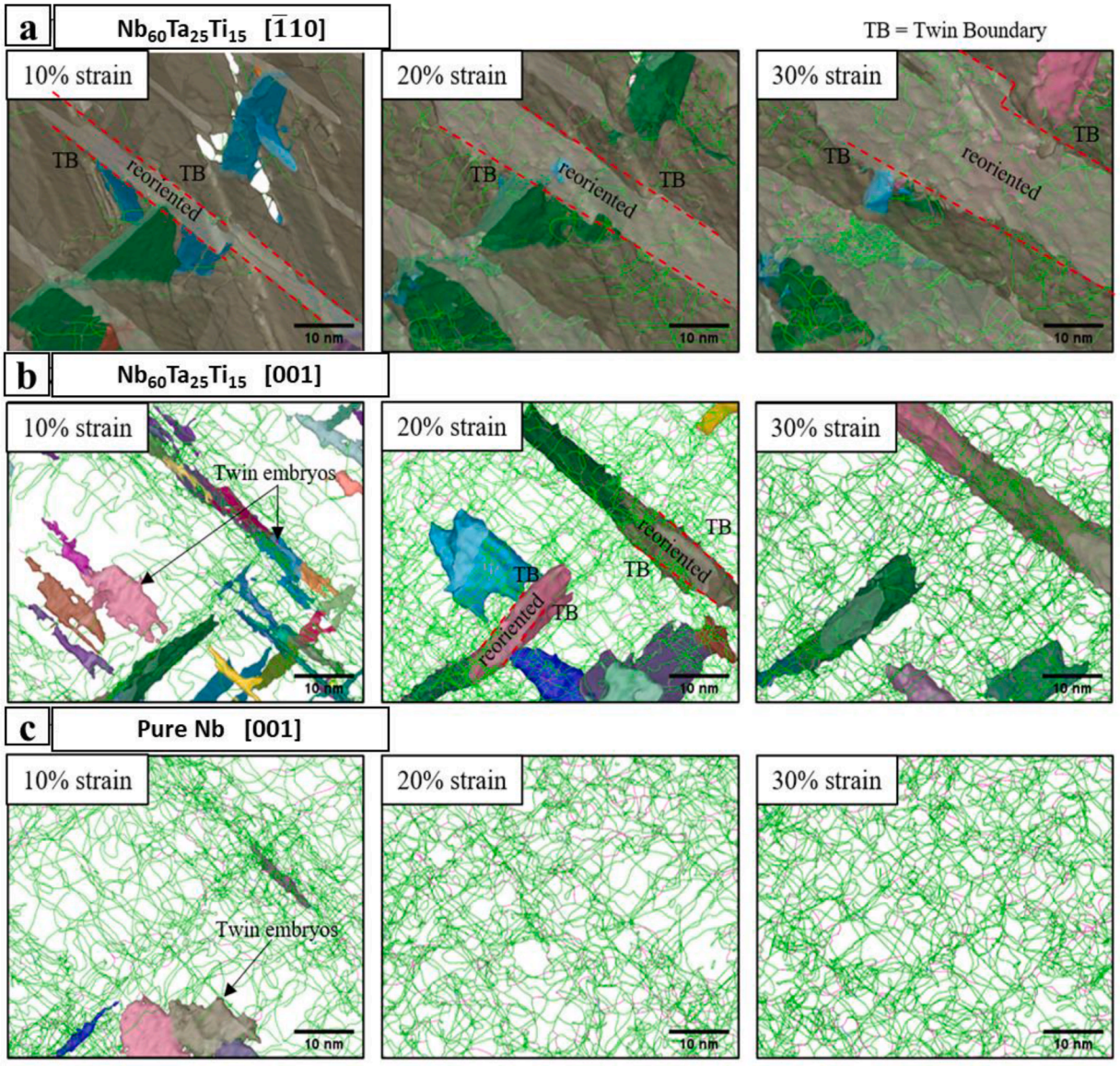

Fig. 8. Structural evolution response to compression. (a) $Nb_{60}Ta_{25}Ti_{15}$ under compression along [$\bar{1}$10] direction at 10% strain, 20% strain, 30% strain, respectively. From left to right, nucleation of twin embryos, twin propagation, and twin growth to span the simulation volume. (b) $Nb_{60}Ta_{25}Ti_{15}$ under compression along [001] direction. Twin embryos and twin growth within $Nb_{60}Ta_{25}Ti_{15}$. (c) pure Nb under compression along [001] direction, deformation governed by pure dislocation slip. Dislocations appear as green and magenta lines. The twins appear as surface mesh. Different colors represent different lattice orientations generated by grain segmentation algorithm in OVITO.

would limit their further use at elevated temperatures. As for the conventional refractory Nb or Ta-based alloys, the tensile strength of the NTTHZ RHEA is still stronger than most of them in the elevated temperature range studied here. The Nb-based C-3009 shows small decrease at elevated temperatures due to the strong solid-solution strengthening caused by Hf and W, which is also attributing to its high melting point [11]. Similar case can be found in Ta-10W alloy. Apart from strength-ductility synergy at ambient-to-elevated temperatures, this NTTHZ RHEA exhibits ultrahigh yield strength (~1.4 GPa) and good ductility (uniform elongation ~ 0.1) at cryogenic temperature of −196 °C, as shown in Fig. S11a. $Hf_{15}Nb_{40}Ta_{25}Ti_{15}Zr_5$ RHEA can retain their high strength at elevated temperatures and exhibit considerable ductility at cryogenic conditions, evading the strength–ductility trade-off, as exhibited in Fig. S11b. The elongation-at-failure of the current $Hf_{15}Nb_{40}Ta_{25}Ti_{15}Zr_5$ RHEA remains in excess of 10% for all testing conditions, which represents a notable accomplishment for RHEAs. Therefore, this strong and ductility RHEA can be used for applications in a wide operating temperature range. $Hf_{15}Nb_{40}Ta_{25}Ti_{15}Zr_5$ RHEA shows comparable tensile properties to HfNbTaTiZr RHEA from −196 °C to ambient temperature [24–28,30,67], as shown in Supplementary Table 2. The melting point of $Hf_{15}Nb_{40}Ta_{25}Ti_{15}Zr_5$ is higher than that of HfNbTaTiZr RHEA, indicating better performance at elevated temperatures [11].

4.3. Deformation mechanism in heterogeneous-structured RHEAs

To elucidate the strengthening mechanisms that are responsible for the observed high strength and high ductility of $Hf_{15}Nb_{40}Ta_{25}Ti_{15}Zr_5$ RHEA with HL structure at ambient temperature, "loading-unloading-reloading" (LUR) cyclic tensile tests were conducted to calculate the internal back-stress, as shown in Fig. S12. Due to the existence of back-stress, the hysteresis loop increases with increasing strain, known as the Bauschinger effect [36]. Following the work of Wu et al., back-stress can be expressed as the average value of yield stresses during the unloading

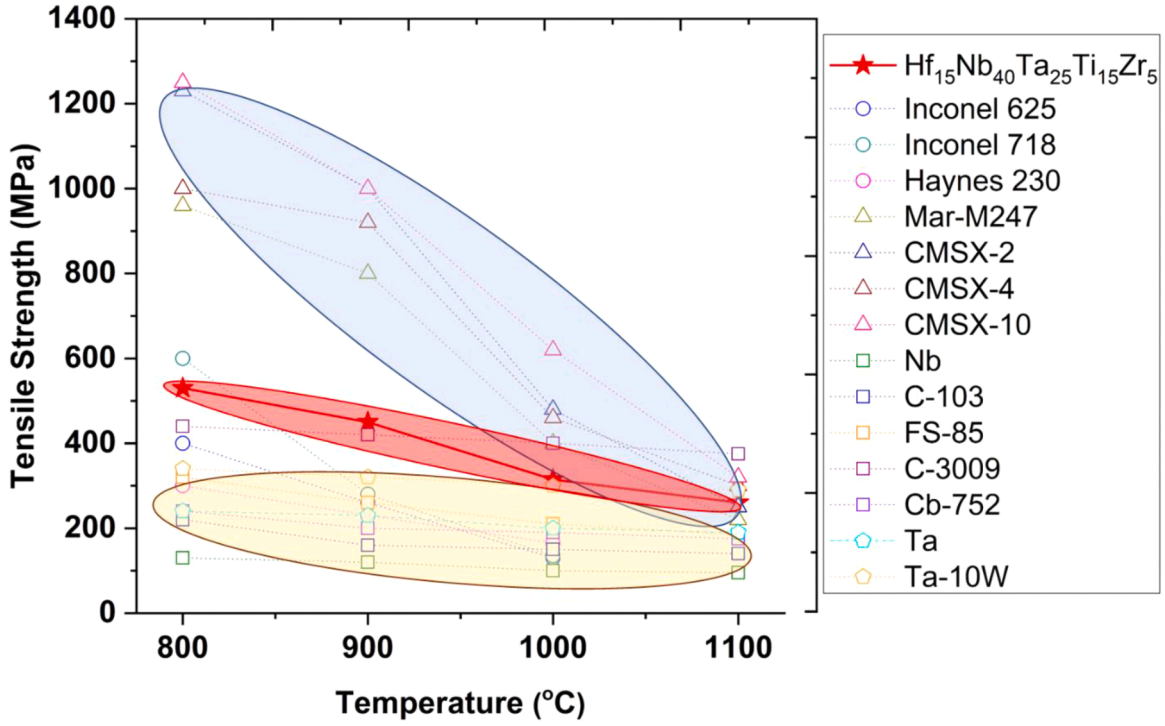

Fig. 9. Tensile strength versus the testing temperatures of $Hf_{15}Nb_{40}Ta_{25}Ti_{15}Zr_5$ with HL structure compared with those of ductile high-temperature metals and alloys, including conventional Ni-based superalloys [60–65], refractory metals (Nb, Ta) [61], and refractory Nb-based alloys and Ta-based alloys [61,66]. Blue and yellow shadow is for the strength range of superalloys (blade use) and refractory metallic materials at elevated temperatures, respectively.

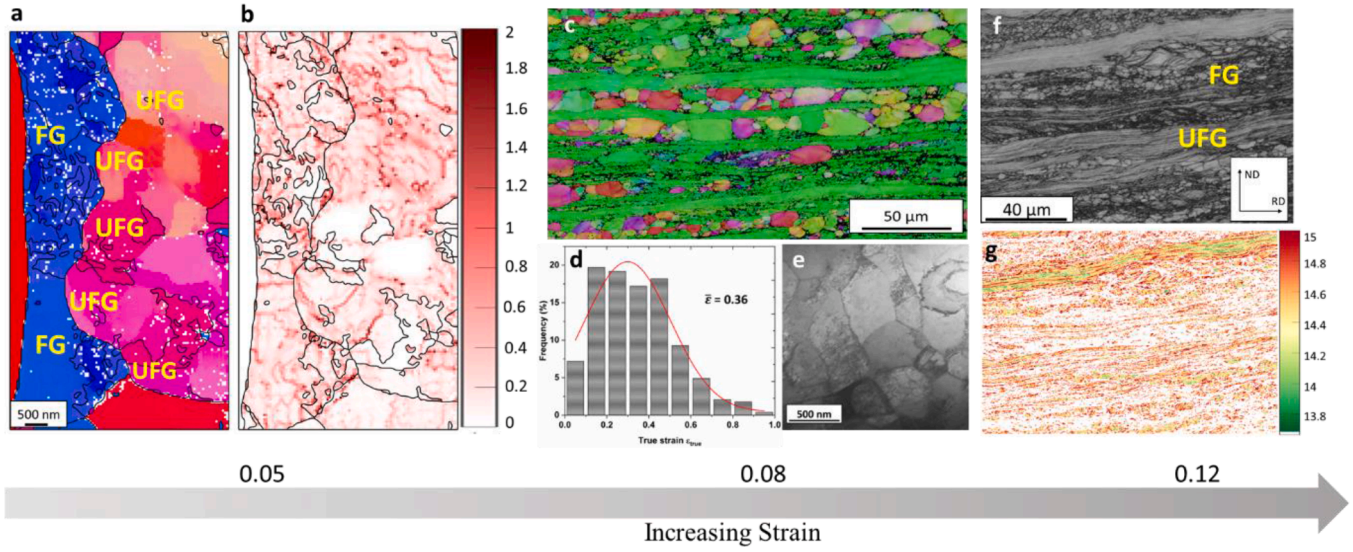

Fig. 10. Deformation mechanisms of $Hf_{15}Nb_{40}Ta_{25}Ti_{15}Zr_5$ RHEA with HL structure at different plastic stages. (a) TEM precession electron diffraction (PED) IPF for deformed $Hf_{15}Nb_{40}Ta_{25}Ti_{15}Zr_5$ RHEA with strain of 0.05. (b) Corresponding kernel average misorientation map (KAM) taken from the deformed specimen in (a), showing a higher strain localization and stronger dislocation activities along interfaces, unit: degree; (c) EBSD IPF image showing most fine grains are elongated along tensile direction at a strain of 0.08; (d) Distribution of strains in fine grains with an average true strain of 0.36 when the HL specimen is deformed to a strain of 0.08; (e) TEM micrograph showing equiaxed ultrafine grains in the HL specimen with a strain of 0.08; (f) EBSD band contrast (BC) micrograph of $Hf_{15}Nb_{40}Ta_{25}Ti_{15}Zr_5$ with strain of 0.12. (g) EBSD-based grain average GND density map corresponding to (f), showing a significant heterogeneous distribution of dislocation density, unit: $\log_{10}(m^{-2})$.

and reloading process [68]. Fig. S12b shows back-stress increases rapidly when plastic deformation occurs, and when comparing with effective stress, back-stress contributes more to strengthening. The precession electron diffraction (PED) image (Fig. 10a,b) taken from the deformed HL-NTTHZ sample with plastic strain of 0.05 clearly demonstrates grain misorientation, which is clear evidence of strain partitioning caused by the strain gradient between UFG and FG. Such strain partitioning leads to the generation of dislocations in FG regions, and pile-ups of dislocations gives rise to work hardening by the combination of generating long-range back stresses and creating obstacles for slip [35]. The EBSD IPF image in Fig. 10c shows that most of fine grains are elongated when the HL specimen is applied with a global

strain of 0.08. The true strain in each grain can be calculated from its aspect ratio α as $\varepsilon = \left(\frac{2}{3}\right)\ln\alpha$, where $\alpha = w/l$, w and l is the width and length of the fine grain, respectively [36]. The average true strain in fine grains is calculated as 0.36, as shown in Fig. 10d. Meanwhile, most ultrafine grains remain equiaxed at the strain of 0.08 (see Fig. 10e). This difference in plastic strain between fine grains (strain = 0.36 > 0.08) and ultrafine grains (strain < 0.08) gives rise to plastic strain partitioning. The plastic deformation has to be continuous at the FG/UFG interfaces, which further causes strain gradient near these interfaces. Accommodation of such strain gradient requires the generation of geometrically necessary dislocations (GNDs) [69,70]. As a consequence, long-range back stresses are created and essentially work as a strain hardening mechanism. Microscopically, back-stress can be mapped indirectly by the density of GNDs, which can be computed from the lattice orientation gradients measured during post-deformed EBSD experiments [71,72]. GND density can be averaged for every grain to present the influence of the heterogeneous grain structure [73,74]. When comparing with GND density of samples before tensile deformation (see Fig. S13), a significant increase of GND density, approximately one order of magnitude higher, appears in the deformed HL specimen, as shown in Fig. 10f,g. The heterogeneous grain structure in Fig. 10f leads to considerably non-uniform distribution of local strain, which gives rise to the heterogeneity of GND density distribution. In Fig. 10g, yellow or red color representing high GND density that lies in the UFG domains, while a green coloring signifying low GND density primarily found in the FG regions, suggesting that FG areas undergo a relatively uniform strain with no large strain gradients along the interfaces. At the same time, ultrafine grains neighboring the UFG/FG boundaries undergo plastic deformation with higher geometric constraints, which leads to a higher strain gradient and higher GND density. However, some lamella composed of UFG act as coarse grains during the plastic deformation, where lower GND density is distributed. The above TEM PED work with kernel average misorientation map (KAM), TEM micrographs of dislocation distribution, and the EBSD-based GND density calculation, confirm the effect of back-stress strengthening on the improvement of the mechanical properties of our HL- NTTHZ RHEA specimen at different stages during plastic deformation. For $Hf_{15}Nb_{40}Ta_{25}Ti_{15}Zr_5$ RHEA samples tested at elevated temperatures, it is found that HL structure can be retained after tensile tests at 800 and 900 °C. However, the specimen is close to completed recrystallization after deformation at 1000°C, as shown in Fig. S14.

5. Conclusion

In summary, a novel refractory HEA was designed and fabricated, with excellent processibility that can be severely cold worked at room temperature directly from the as-cast state without intermediate annealing. The surface defects caused by the solidification can be eliminated by the cold rolling process itself. It is postulated that the deformation-induced twins and microbands formed during the cold-rolling process are responsible for this self-healing phenomenon. The formation mechanism of deformation-induced twins is confirmed by MD simulation analysis. The excellent cold-workability allows this RHEA to have tunable microstructure in the subsequent annealing step. Dislocation pipe diffusion significantly increases the diffusion rate, making this RHEA homogeneous in an energy and time efficient way, a true achievement for an ultra-high melting point alloy. We have also demonstrated experimentally that our $Hf_{15}Nb_{40}Ta_{25}Ti_{15}Zr_5$ RHEA is both strong and ductile at cryogenic-to-elevated temperatures. Back-stress strengthening contributes to the high tensile strength of hetero-structured $Hf_{15}Nb_{40}Ta_{25}Ti_{15}Zr_5$ RHEA at ambient temperature. Our NbTaTi-based refractory HEA design strategy provides a practical way to design and fabricate metallic materials with ultra-high melting points and excellent processibility.

Data availability

The data that support the findings of this study are available within the paper and the Supplementary Information, and all data are available from the authors on reasonable request.

Declaration of Competing Interest

The authors declare that they have no known competing financial interests or personal relationships that could have appeared to influence the work reported in this paper.

Acknowledgments

C.Z., BEM and E.J.L. would like to acknowledge financial support from UCI. This research was also partially supported (EJL, X.W., BEM and TJR) by the National Science Foundation Materials Research Science and Engineering Center program through the UC Irvine Center for Complex and Active Materials (DMR-2011967). Xinyi W. and P.C. acknowledge financial support from National Science Foundation (DMR-2105328, CMMI-1935371). We also would like to thank Dr. Fan Ye, Dr. Li. Xing, and Dr. Jian-guo Zheng (IMRI, UC Irvine) for TEM assistance. We acknowledge Dr. Mingde Qin and Xiao Liu (UC San Diego) for assistance in some experiments.

Supplementary materials

Supplementary material associated with this article can be found, in the online version, at doi:10.1016/j.actamat.2022.118602.

References

[1] Y. Zhang, T.T. Zuo, Z. Tang, M.C. Gao, K.A. Dahmen, P.K. Liaw, Z.P. Lu, Microstructures and properties of high-entropy alloys, Prog. Mater. Sci. 61 (2014) 1–93.
[2] D.B. Miracle, O.N. Senkov, A critical review of high entropy alloys and related concepts, Acta Mater. 122 (2017) 448–511.
[3] E.P. George, D. Raabe, R.O. Ritchie, High-entropy alloys, Nat. Rev. Mater. 1 (2019).
[4] T. Yang, Y.L. Zhao, Y. Tong, Z.B. Jiao, J. Wei, J.X. Cai, X.D. Han, D. Chen, A. Hu, J. J. Kai, Multicomponent intermetallic nanoparticles and superb mechanical behaviors of complex alloys, Science 362 (2018) 933–937.
[5] Z. Fu, L. Jiang, J.L. Wardini, B.E. MacDonald, H. Wen, W. Xiong, D. Zhang, Y. Zhou, T.J. Rupert, W. Chen, A high-entropy alloy with hierarchical nanoprecipitates and ultrahigh strength, Sci. Adv. 4 (2018) eaat8712.
[6] J.Y. He, H. Wang, H.L. Huang, X.D. Xu, M.W. Chen, Y. Wu, X.J. Liu, T.G. Nieh, K. An, Z.P. Lu, A precipitation-hardened high-entropy alloy with outstanding tensile properties, Acta Mater. 102 (2016) 187–196.
[7] B. Gludovatz, A. Hohenwarter, D. Catoor, E.H. Chang, E.P. George, R.O. Ritchie, A fracture-resistant high-entropy alloy for cryogenic applications, Science 345 (2014) 1153–1158.
[8] O.N. Senkov, D.B. Miracle, K.J. Chaput, J.P. Couzinie, Development and exploration of refractory high entropy alloys—a review, J. Mater. Res. 33 (2018) 3092–3128.
[9] C. Lee, G. Kim, Y. Chou, B.L. Musicó, M.C. Gao, K. An, G. Song, Y.C. Chou, V. Keppens, W. Chen, Temperature dependence of elastic and plastic deformation behavior of a refractory high-entropy alloy, Sci. Adv. 6 (2020) eaaz4748.
[10] F. Maresca, W.A. Curtin, Mechanistic origin of high strength in refractory BCC high entropy alloys up to 1900K, Acta Mater. 182 (2020) 235–249.
[11] O.N. Senkov, S. Gorsse, D.B. Miracle, High temperature strength of refractory complex concentrated alloys, Acta Mater. 175 (2019) 394–405.
[12] Y. Zou, S. Maiti, W. Steurer, R. Spolenak, Size-dependent plasticity in an Nb25Mo25Ta25W25 refractory high-entropy alloy, Acta Mater. 65 (2014) 85–97.
[13] Y. Zou, H. Ma, R. Spolenak, Ultrastrong ductile and stable high-entropy alloys at small scales, Nat. Commun. 6 (2015) 1–8.
[14] S. Wei, S.J. Kim, J. Kang, Y. Zhang, Y. Zhang, T. Furuhara, E.S. Park, C.C. Tasan, Natural-mixing guided design of refractory high-entropy alloys with as-cast tensile ductility, Nat. Mater. (2020) 1–7.
[15] H. Huang, Y. Wu, J. He, H. Wang, X. Liu, K. An, W. Wu, Z. Lu, Phase-transformation ductilization of brittle high-entropy alloys via metastability engineering, Adv. Mater. 29 (2017), 1701678.
[16] O.N. Senkov, G.B. Wilks, D.B. Miracle, C.P. Chuang, P.K. Liaw, Refractory high-entropy alloys, Intermetallics 18 (2010) 1758–1765.
[17] O.N. Senkov, D.B. Miracle, S.I. Rao, Correlations to improve room temperature ductility of refractory complex concentrated alloys, Mater. Sci. Eng. A 820 (2021), 141512.

[18] Y.C. Huang, Y.C. Lai, Y.H. Lin, S.K. Wu, A study on the severely cold-rolled and annealed quaternary equiatomic derivatives from quinary HfNbTaTiZr refractory high entropy alloy, J. Alloy. Compd. 855 (2021), 157404.
[19] S. Sheikh, S. Shafeie, Q. Hu, J. Ahlström, C. Persson, J. Veselý, J. Zýka, U. Klement, S. Guo, Alloy design for intrinsically ductile refractory high-entropy alloys, J. Appl. Phys. 120 (2016), 164902.
[20] L. Lilensten, J.P. Couzinié, J. Bourgon, L. Perrière, G. Dirras, F. Prima, I. Guillot, Design and tensile properties of a bcc Ti-rich high-entropy alloy with transformation-induced plasticity, Mater. Res. Lett. 5 (2017) 110–116.
[21] S.P. Wang, E. Ma, J. Xu, New ternary equi-atomic refractory medium-entropy alloys with tensile ductility: Hafnium versus titanium into NbTa-based solution, Intermetallics 107 (2019) 15–23.
[22] J. Zýka, J. Málek, J. Veselý, F. Lukáč, J. Čížek, J. Kuriplach, O. Melikhova, Microstructure and room temperature mechanical properties of different 3 and 4 element medium entropy alloys from HfNbTaTiZr system, Entropy 21 (2019) 114.
[23] Z. An, S. Mao, T. Yang, C.T. Liu, B. Zhang, E. Ma, H. Zhou, Z. Zhang, L. Wang, X. Han, Spinodal-modulated solid solution delivers a strong and ductile refractory high-entropy alloy, Mater. Horiz. 8 (2021) 948–955.
[24] O.N. Senkov, S.L. Semiatin, Microstructure and properties of a refractory high-entropy alloy after cold working, J. Alloy. Compd. 649 (2015) 1110–1123.
[25] O.N. Senkov, A.L. Pilchak, S.L. Semiatin, Effect of cold deformation and annealing on the microstructure and tensile properties of a HfNbTaTiZr refractory high entropy alloy, Metall. Mater. Trans. A 49 (2018) 2876–2892.
[26] S. Chen, K.K. Tseng, Y. Tong, W. Li, C.W. Tsai, J.W. Yeh, P.K. Liaw, Grain growth and Hall-Petch relationship in a refractory HfNbTaZrTi high-entropy alloy, J. Alloy. Compd. 795 (2019) 19–26.
[27] B. Schuh, B. Völker, J. Todt, N. Schell, L. Perrière, J. Li, J.P. Couzinié, A. Hohenwarter, Thermodynamic instability of a nanocrystalline, single-phase TiZrNbHfTa alloy and its impact on the mechanical properties, Acta Mater. 142 (2018) 201–212.
[28] C.C. Juan, M.H. Tsai, C.W. Tsai, W.L. Hsu, C.M. Lin, S.K. Chen, S.J. Lin, J.W. Yeh, Simultaneously increasing the strength and ductility of a refractory high-entropy alloy via grain refining, Mater. Lett. 184 (2016) 200–203.
[29] S. Zherebtsov, N. Yurchenko, D. Shaysultanov, M. Tikhonovsky, G. Salishchev, N. Stepanov, Microstructure and mechanical properties evolution in HfNbTaTiZr refractory high-entropy alloy during cold rolling, Adv. Eng. Mater. 22 (2020), 2000105.
[30] R.R. Eleti, N. Stepanov, S. Zherebtsov, Mechanical behavior and thermal activation analysis of HfNbTaTiZr body-centered cubic high-entropy alloy during tensile deformation at 77 K, Scr. Mater. 188 (2020) 118–123.
[31] F. Lukáč, M. Dudr, J. Čížek, P. Harcuba, T. Vlasák, M. Janeček, J. Kuriplach, J. Moon, H.S. Kim, J. Zýka, Defects in high entropy alloy HfNbTaTiZr prepared by high pressure torsion, Acta Phys. Pol. A 134 (2018) 891–894.
[32] R.R. Eleti, V. Raju, M. Veerasham, S.R. Reddy, P.P. Bhattacharjee, Influence of strain on the formation of cold-rolling and grain growth textures of an equiatomic HfZrTiTaNb refractory high entropy alloy, Mater. Charact. 136 (2018) 286–292.
[33] J. Čížek, P. Haušild, M. Cieslar, O. Melikhova, T. Vlasák, M. Janeček, R. Král, P. Harcuba, F. Lukáč, J. Zýka, Strength enhancement of high entropy alloy HfNbTaTiZr by severe plastic deformation, J. Alloy. Compd. 768 (2018) 924–937.
[34] Y. Zhu, K. Ameyama, P.M. Anderson, I.J. Beyerlein, H. Gao, H.S. Kim, E. Lavernia, S. Mathaudhu, H. Mughrabi, R.O. Ritchie, Heterostructured materials: superior properties from hetero-zone interaction, Mater. Res. Lett. 9 (2021) 1–31.
[35] E. Ma, T. Zhu, Towards strength–ductility synergy through the design of heterogeneous nanostructures in metals, Mater. Today 20 (2017) 323–331.
[36] X. Wu, M. Yang, F. Yuan, G. Wu, Y. Wei, X. Huang, Y. Zhu, Heterogeneous lamella structure unites ultrafine-grain strength with coarse-grain ductility, Proc. Natl. Acad. Sci. 112 (2015) 14501–14505.
[37] Y. Wang, M. Chen, F. Zhou, E. Ma, High tensile ductility in a nanostructured metal, Nature 419 (2002) 912.
[38] V.L. Tellkamp, E.J. Lavernia, A. Melmed, Mechanical behavior and microstructure of a thermally stable bulk nanostructured Al alloy, Metall. Mater. Trans. A 32 (2001) 2335–2343.
[39] K. Lu, Making strong nanomaterials ductile with gradients, Science 345 (2014) 1455–1456.
[40] Z. Cheng, H. Zhou, Q. Lu, H. Gao, L. Lu, Extra strengthening and work hardening in gradient nanotwinned metals, Science 362 (2018) eaau1925.
[41] E. Ma, X. Wu, Tailoring heterogeneities in high-entropy alloys to promote strength–ductility synergy, Nat. Commun. 10 (2019) 1–10.
[42] C. Zhang, C. Zhu, T. Harrington, K. Vecchio, Design of non-equiatomic high entropy alloys with heterogeneous lamella structure towards strength-ductility synergy, Scr. Mater. 154 (2018) 78–82.
[43] C. Zhang, C. Zhu, P. Cao, X. Wang, F. Ye, K. Kaufmann, L. Casalena, B. E. MacDonald, X. Pan, K. Vecchio, E.J. Lavernia, Aged metastable high-entropy alloys with heterogeneous lamella structure for superior strength-ductility synergy, Acta Mater. 199 (2020) 602–612.
[44] Y. Murakami. Stress intensity factors, Pergamon, 1987.
[45] F. Jiang, K.S. Vecchio, Fracture of nitinol under quasistatic and dynamic loading, Metall. Mater. Trans. A. 38 (2007) 2907–2915.
[46] S. Sulzer, E. Alabort, A. Németh, B. Roebuck, R. Reed, On the rapid assessment of mechanical behavior of a prototype nickel-based superalloy using small-scale testing, Metall. Mater. Trans. A 49 (2018) 4214–4235.
[47] X.W. Zhou, R.A. Johnson, H.N.G. Wadley, Misfit-energy-increasing dislocations in vapor-deposited CoFe/NiFe multilayers, Phys. Rev. B 69 (2004), 144113.
[48] D.Y. Lin, S.S. Wang, D.L. Peng, M. Li, X.D. Hui, An n-body potential for a Zr–Nb system based on the embedded-atom method, J. Phys. Condens. Matter 25 (2013), 105404.
[49] A. Stukowski, Visualization and analysis of atomistic simulation data with OVITO–the open visualization tool, Model. Simul. Mater. Sci. Eng. 18 (2009) 15012.
[50] O.N. Senkov, J.M. Scott, S.V Senkova, F. Meisenkothen, D.B. Miracle, C. F. Woodward, Microstructure and elevated temperature properties of a refractory TaNbHfZrTi alloy, J. Mater. Sci. 47 (2012) 4062–4074.
[51] C. Zhang, C. Zhu, K. Vecchio, Non-equiatomic FeNiCoAl-based high entropy alloys with multiscale heterogeneous lamella structure for strength and ductility, Mater. Sci. Eng. A 743 (2019) 361–371.
[52] D.A. Hughes, N. Hansen, Microstructure and strength of nickel at large strains, Acta Mater. 48 (2000) 2985–3004.
[53] S. Sadeghpour, S.M. Abbasi, M. Morakabati, L.P. Karjalainen, Effect of dislocation channeling and kink band formation on enhanced tensile properties of a new beta Ti alloy, J. Alloy. Compd. 808 (2019), 151741.
[54] Y. Yang, S.Q. Wu, G.P. Li, Y.L. Li, Y.F. Lu, K. Yang, P. Ge, Evolution of deformation mechanisms of Ti–22.4 Nb–0.73 Ta–2Zr–1.34 O alloy during straining, Acta Mater. 58 (2010) 2778–2787.
[55] A.T. Churchman, The yield phenomena, kink bands and geometric softening in titanium crystals, Acta Metall. 3 (1955) 22–29.
[56] P. Shewmon, Diffusion in Solids, Springer, 2016.
[57] Z. Balogh, G. Schmitz, Diffusion in metals and alloys. Physical Metallurgy, Elsevier, 2014, pp. 387–559.
[58] S. Maiti, W. Steurer, Structural-disorder and its effect on mechanical properties in single-phase TaNbHfZr high-entropy alloy, Acta Mater. 106 (2016) 87–97.
[59] Z. Lei, X. Liu, Y. Wu, H. Wang, S. Jiang, S. Wang, X. Hui, Y. Wu, B. Gault, P. Kontis, Enhanced strength and ductility in a high-entropy alloy via ordered oxygen complexes, Nature 563 (2018) 546.
[60] R.C. Reed, The Superalloys: Fundamentals and Applications, Cambridge University Press, 2008.
[61] N.E. Prasad, R.J.H. Wanhill, Aerospace Materials and Material Technologies, Springer, 2017.
[62] M. Kaufman, Properties of cast Mar-M-247 for turbine blisk applications, Superalloys 1984 (1984) 43–52.
[63] A. Sengupta, S.K. Putatunda, L. Bartosiewicz, J. Hangas, P.J. Nailos, M. Peputapeck, F.E. Alberts, Tensile behavior of a new single-crystal nickel-based superalloy (CMSX-4) at room and elevated temperatures, J. Mater. Eng. Perform. 3 (1994) 73–81.
[64] G.L. Erickson, The development and application of CMSX-10, Superalloys 1996 (1996) 35–44.
[65] S. Wee, J. Do, K. Kim, C. Lee, C. Seok, B.G. Choi, Y. Choi, W. Kim, Review on mechanical thermal properties of superalloys and thermal barrier coating used in gas turbines, Appl. Sci. 10 (2020) 5476.
[66] C.C. Wojcik, W. Chang, Thermomechanical processing and properties of niobium alloys, in:, in: Proceedings of the International Symposium Niobium 2001, 2001, pp. 163–173.
[67] S. Wang, M. Wu, D. Shu, G. Zhu, D. Wang, B. Sun, Mechanical instability and tensile properties of TiZrHfNbTa high entropy alloy at cryogenic temperatures, Acta Mater. 201 (2020) 517–527.
[68] M. Yang, Y. Pan, F. Yuan, Y. Zhu, X. Wu, Back stress strengthening and strain hardening in gradient structure, Mater. Res. Lett. 4 (2016) 145–151.
[69] M.F. Ashby, The deformation of plastically non-homogeneous materials, Philos. Mag. 21 (1970) 399–424.
[70] H. Gao, Y. Huang, Geometrically necessary dislocation and size-dependent plasticity, Scr. Mater. 48 (2003) 113–118.
[71] C. Zhu, T. Harrington, V. Livescu, G.T. Gray, K.S. Vecchio, Determination of geometrically necessary dislocations in large shear strain localization in aluminum, Acta Mater. 118 (2016) 383–394.
[72] C. Zhu, T. Harrington, G.T. Gray, K.S. Vecchio, Dislocation-type evolution in quasi-statically compressed polycrystalline nickel, Acta Mater. 155 (2018) 104-116.
[73] C. Zhu, V. Livescu, T. Harrington, O. Dippo, G.T. Gray, K.S. Vecchio, Investigation of the shear response and geometrically necessary dislocation densities in shear localization in high-purity titanium, Int. J. Plast. 92 (2017) 148–163.
[74] E. Demir, D. Raabe, N. Zaafarani, S. Zaefferer, Investigation of the indentation size effect through the measurement of the geometrically necessary dislocations beneath small indents of different depths using EBSD tomography, Acta Mater. 57 (2009) 559–569.